Supporting Information

The Contrasting Impacts of Polyethylene Glycol on Electrochemical Behaviors of Fe and Zn Metal Anodes in Aqueous Batteries

Sungjin Yang,[a,d] Cheng Chen,[a,d] Xingyi Lyu,[b] Soenke Seifert,[c] Hunter Maclennan,[a] Min Soo Jung,[a] Emmanuel Nyela Musa,[a] Yiming Sui,[a] Alexis M. Scida,[a] Riitvek Baddireddi,[a] Maxine A. McNerney,[a] Kyriakos Stylianou,[a] Tao Li,*[b,c] Chong Fang,*[a] Xiulei Ji*[a]

[a] Department of Chemistry, Oregon State University, Corvallis, Oregon, 97331-4003, United States
Email : david.ji@oregonstate.edu chong.fang@oregonstate.edu

[b] Department of Chemistry and Biochemistry, Northen Illinois University, DeKalb, Illinois 60115, United States
Email : tli4@niu.edu

[c] X-ray Science Division, Argonne National Laboratory, Lemont, Illinois 60439, United States

[d] These authors contributed equally.

Material Preparation

The Ti foil with a thickness of 10 μm was obtained from Shaanxi Titanium Aviation New Material Technology. The Fe foil, measuring 500 μm thick, was sourced from Amazon. Zn foil of different thicknesses (100 μm and 250 μm) was acquired from Alibaba and Thermo Scientific, respectively. Anhydrous zinc chloride (99.95%) was purchased from Thermo Scientific. Zinc acetate dihydrate (ACS reagent, 98.0 – 101.0 %), anhydrous zinc bromide (98%), and copper(II) chloride dihydrate (99 %) were sourced from Alfa Aesar. Zinc trifluoromethanesulfonate (98%) was obtained from Acros Organics. Manganese(II) chloride tetrahydrate (≥99%) and manganese powder (325 mesh, ≥99%) were acquired from Sigma Aldrich. Polyethylene Glycol 200 was purchased from TCI chemicals. Iron(II) chloride tetrahydrate ($FeCl_2 \cdot 4H_2O$, ≥99%) from Thermo Scientific was stored in an argon-filled glove box to prevent oxidation. HPLC-grade water (Sigma Aldrich) was purged with argon gas for 30 minutes to remove dissolved oxygen before being transferred to the argon-filled glove box. Electrolytes containing $FeCl_2$ were prepared and maintained within the argon-filled glove box.

Materials Characterization

Hydrogen evolution reaction (HER) measurements were performed using a PerkinElmer Clarus 480 gas chromatography (GC), which featured a 5 Å molecular sieve column with Ar as the carrier gas and a thermal conductivity detector. For the GC analysis of Fe metal anode (FeMA), we assembled Ti || Fe asymmetric Swagelok cells with 10 μm Ti foil and 500 μm Fe foil, operating at a current density of 1 mA cm^{-2} for 50 cycles.

The FSRS setup incorporated a mode-locked Ti:sapphire oscillator (Mantis-5, Coherent, Inc.) that seeds a regenerative amplifier (Legend Elite USP-1K-HE, Coherent, Inc.), producing a fundamental laser pulse train with a center wavelength of approximately 800 nm, a pulse duration of 35 fs, and an average power of 3.6 W at a repetition rate of 1 kHz. The picosecond (ps) Raman pump was generated using a home-built three-stage noncollinear optical parametric amplifier system: one stage plus a spectral filter for the ps seed and two stages for the amplification by a ps 400 nm pulse produced by a home-built second harmonic bandwidth compressor (SHBC). The Raman pump at 510 nm with an average power of 4–5 mW was used for FSRS data collection in the electronic ground state (GS, S_0). The fs Raman probe was produced by focusing a small portion of the 800 nm fundamental pulse onto a 2-mm-thick quartz cuvette (Spectrosil 1-Q-2, Starna Cells) filled with deionized water, followed by temporal compression using a pair of chirped mirrors (DMC-9, 450–950 nm, Laser Quantum). Both the Raman pump and probe pulses were then focused by a reflective parabolic mirror onto a 1-mm-thick quartz cuvette (Spectrosil 1-Q-1, Starna Cells) containing various electrolyte samples. After passing through the sample, the probe was collimated, refocused and dispersed by a reflective grating (1200 grooves per mm selected) inside a spectrograph (IsoPlane SCT-320, Princeton Instruments), ultimately being imaged at the exit plane onto a CCD array camera (PIXIS:100F, Princeton Instruments). All the spectral data were collected on the Stokes side (with a redder Raman probe than Raman pump) under the same experimental conditions on the same day to minimize the effects of laser fluctuations. The room temperature was ~22 °C. The frequency calibration using cyclohexane solvent was conducted before and after the GS-FSRS measurements, also serving as a reproducibility check.

The SAXS/WAXS experiments for $FeCl_2$ electrolytes with PEG were performed at the 12ID-E station of the Advanced Photon Source at Argonne National Laboratory, using an X-ray energy of 17 keV. A Pilatus 2M detector, positioned approximately 5.1 m downstream from the sample, was used for SAXS measurements, while a Pilatus 900K detector for WAXS was placed about 0.5 m from the sample. The sample-to-detector distances were calibrated using Silver behenate. All samples—including electrolytes and pure solvents—were loaded into 1.5 mm sealed quartz capillaries. Each measurement involved a 1-second exposure at room temperature. For the $ZnCl_2$ electrolytes with PEG, experiments were conducted at the 12-ID-B station of the Advanced Photon Source, with an X-ray energy of 13.3 keV. A Pilatus 2M detector for SAXS was positioned approximately 2 m downstream from the samples. To minimize X-ray absorption by the highly concentrated zinc solution, the standard 1.5 mm capillaries were replaced with 0.3 mm capillaries, and the nozzle was positioned very close to the sample to reduce air scattering.

Electrochemical Measurements

All cells containing $FeCl_2$ electrolytes were assembled in the Argon-filled glove box. The Mn free-standing film was composed of 70 wt% Mn powder, 20 wt% KetjenBlack, and 10 wt% Polytetrafluoroethylene (PTFE) binder, all mixed in isopropanol solvent. The CV, LSV and Tafel plots were collected using a VMP-3 multichannel workstation with three electrode Swagelok cells. The Electrochemical Impedance Spectroscopy (EIS) was performed using the same setup with CV, LSV, and Tafel measurements, but with Ti || Fe asymmetric Swagelok cells. The AC signal with a voltage amplitude of 10 mV was employed to scan the frequency ranging from 100 kHz to 0.1 Hz, with 22 measurement points selected per decade. The galvanostatic charge discharge (GCD) cycling data were gathered using a Landt CT3002AU.

Coulombic efficiency (CE) is calculated for each cycle using the following equation (1):

$$\text{CE (\%)} = \left(\frac{Q_S}{Q_P}\right) \times 100 \tag{1}$$

Here, Q_P represents the capacity of the plating process, and Q_S represents the capacity of the stripping process. This method determines the efficiency at which iron metal is plated on and stripped from the titanium metal substrate in an asymmetrical Ti || Fe cell.

Average CE is calculated according to the following equation (2) instead:[1]

$$\text{CE (\%)} = \left(\frac{nQ_C + Q_S}{nQ_C + Q_T}\right) \times 100 \tag{2}$$

For Fe metal anode (FeMA), Q_T represents charge used to plate iron onto the working electrode as an iron reservoir, Q_C denotes the smaller capacity used to cycle iron between the working and counter electrodes for 49 cycles, and Q_S is the final stripping capacity, indicating the amount of iron remaining after the cycling procedure. We computed the average CE for 5FC and 5FC20PEG electrolytes, with Q_T set at 10.0 mAh and Q_c at 1.0 mAh.

For Zn metal anode (ZMA), we defined Q_T as the total capacity of the Zn foil, which has a thickness of 15 µm, while Q_C represents a fixed percentage (10%) of Q_T. Additionally, Q_S refers to the capacity obtained from the final stripping process after 50 cycles. To accurately measure the average CE using this testing methodology with the existing Zn foil, we calculated the utilization percentage (96.1%), which was incorporated into the Q_T calculation.

When measuring the CE and average CE of the FeMA, we used asymmetric Ti || Fe Swagelok cells, utilizing 10 µm thickness Ti foil as the working electrode and 500 µm thickness Fe foil as the counter electrode. For the average CE of the ZMA, we employed asymmetric Zn || Zn Swagelok cells, where the working electrode was a 15 µm thickness Zn foil and the counter electrode was a 250 µm thickness Zn foil.

To measure the hydrogen gas production for Zn metal anode batteries, Zn||Zn symmetric beaker cells were assembled with 10 µm thickness of Zn foil and tested at a current density of 1 mA cm^{-2} for 50 cycles.

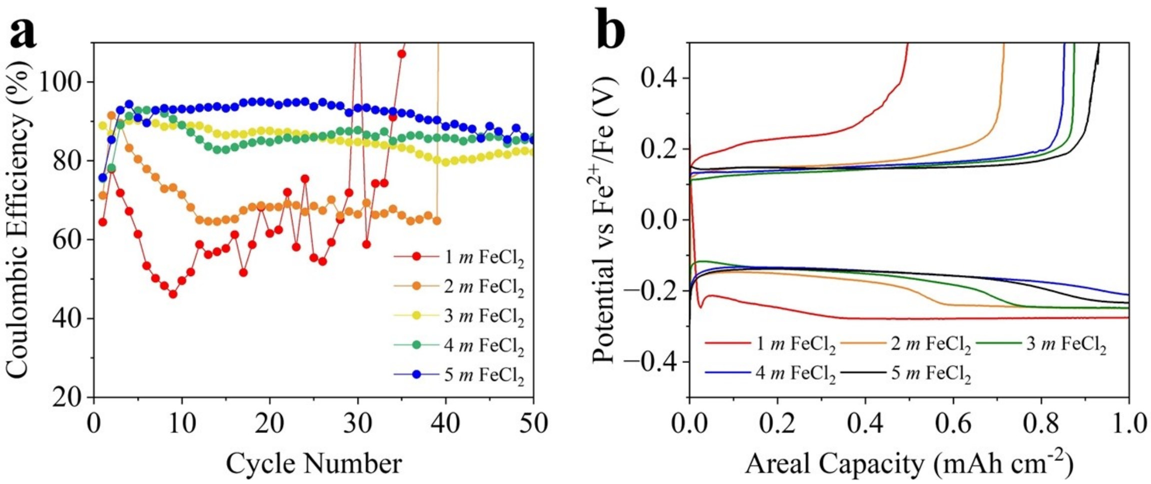

Figure S1. The electrochemical performance of the FeMA at a current density of 1 mA cm^{-2}, with each plating or stripping process lasting for 1 hour. (a) CE tests. (b) GCD profiles for the 10th cycle.

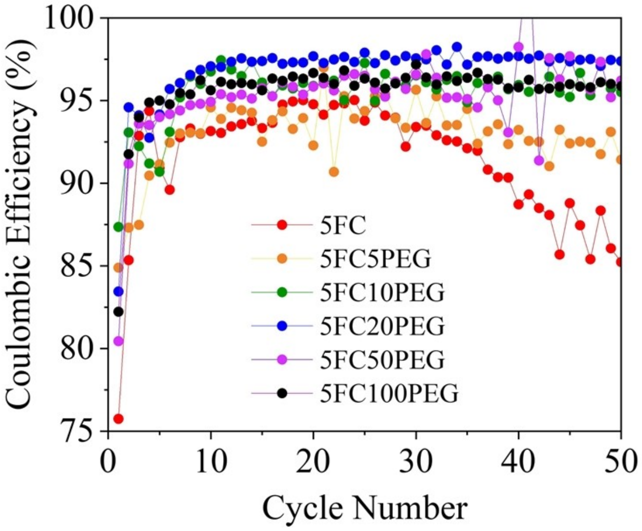

Figure S2. CE test for various electrolytes at a current density of 1 mA cm^{-2}, with each plating or stripping process lasting for 1 hour.

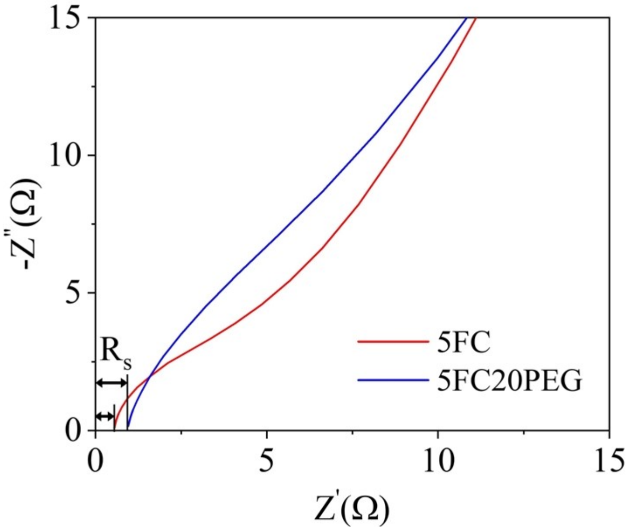

Figure S3. Nyquist plots of 5FC and 5FC20PEG electrolytes.

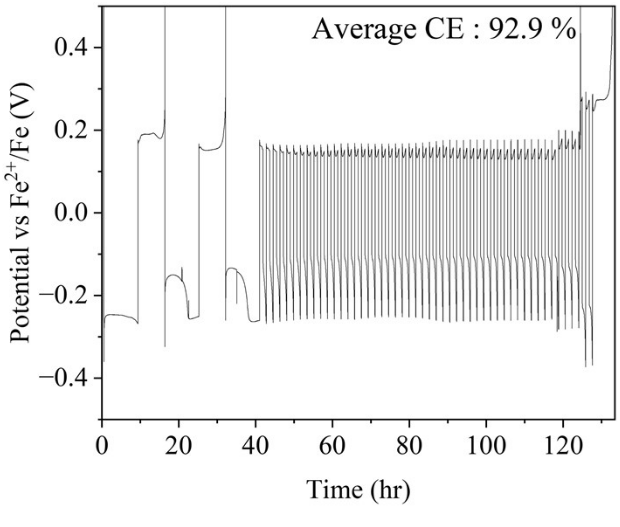

Figure S4. GCD profiles for 5FC electrolyte to determine the average CE at a current density of 1 mA cm^{-2}.

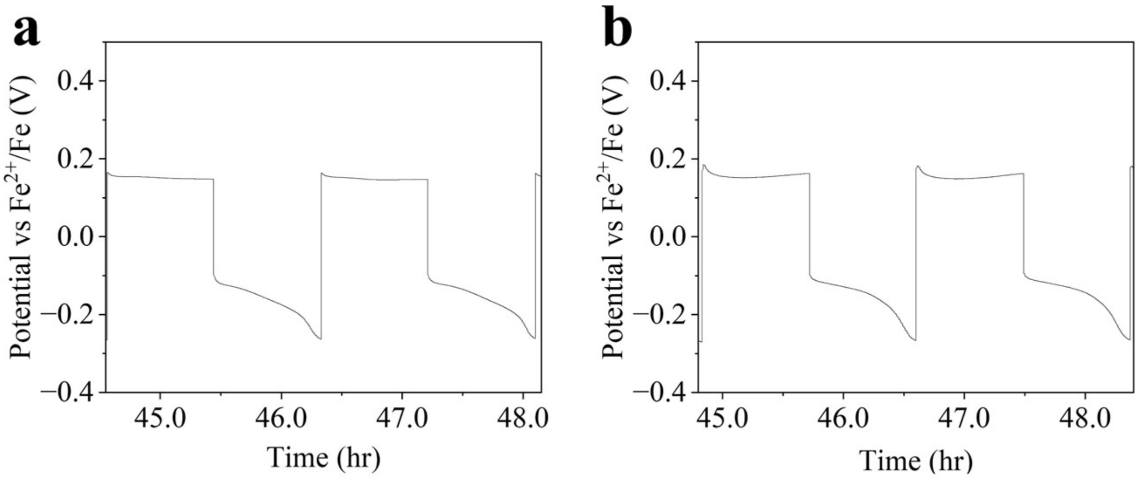

Figure S5. GCD profiles for 5FC (a) and 5FC20PEG (b) electrolytes, respectively, enlarged from Fig. S4 and 1c.

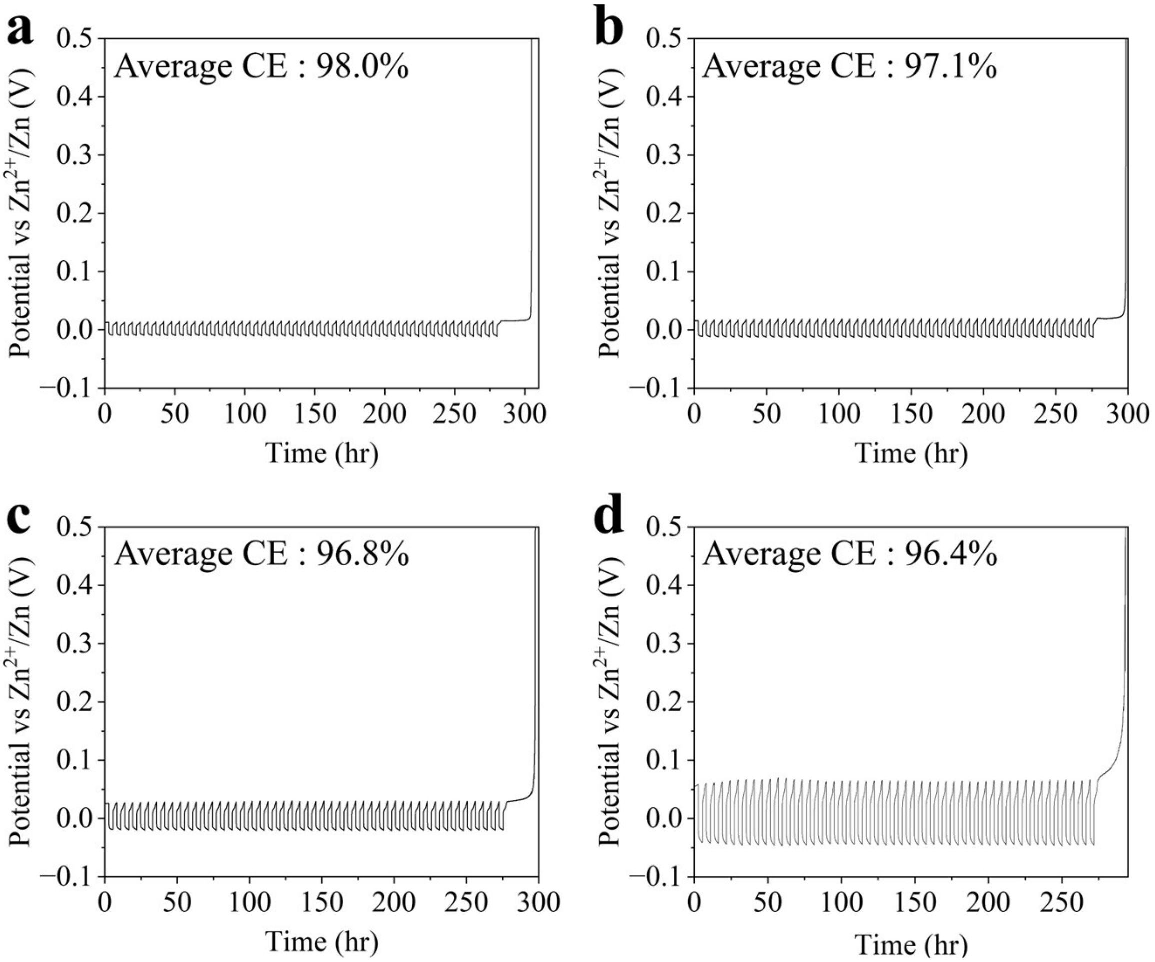

Figure S6. GCD profiles for (a) 30Zn, (b) 30Zn50PEG, (c) 30Zn100PEG, (d) 30Zn200PEG to determine the average CE at a current density of 0.2 mA cm^{-2}.

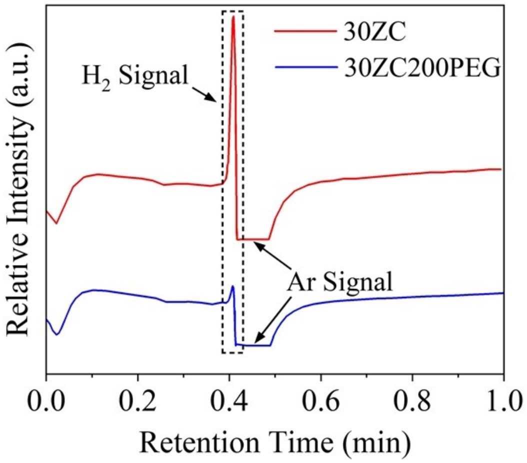

Figure S7. GC profiles of Zn || Zn symmetric beaker cells taken after 50 Galvanostatic plating-stripping cycles at a current density 1 mA cm^{-2} with a capacity of 1 mAh cm^{-2} under an argon carrier gas.

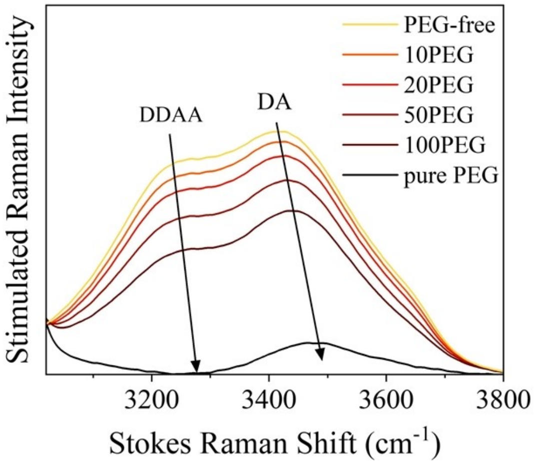

Figure S8. FSRS spectra for water with varying amounts of PEG added.

Furthermore, we have performed new Raman spectroscopy measurements to reveal the impacts of PEG addition to the electrolyte on O-H stretching modes of water, which is telling about the hydrogen-bonding interactions between water molecules (**Fig. S8**). Specifically, the peak corresponding to the DDAA mode of water is weakened as the PEG content increases, which indicates that the dissolved PEG chains penetrate into the ensemble of water molecules, reducing the water-water interactions. Furthermore, the DA mode shifts to higher frequencies (blue-shifted) upon the addition of PEG, implying more stiffened O-H bonds of water molecules. The Raman results are consistent with the reduced HER activity.

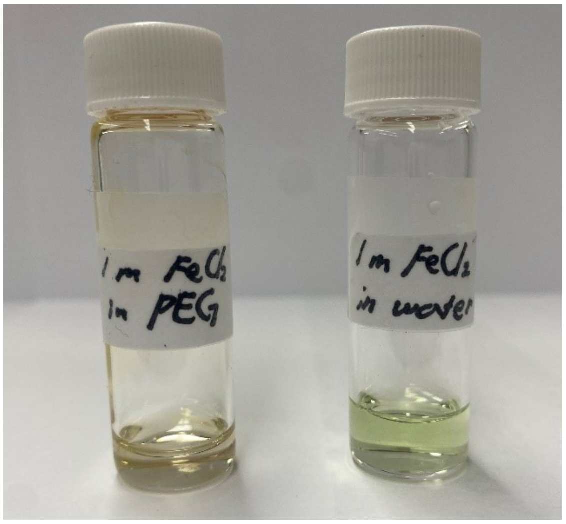

Figure S9. Photograph of the 1 *m* $FeCl_2$ in PEG (left) and water (right).

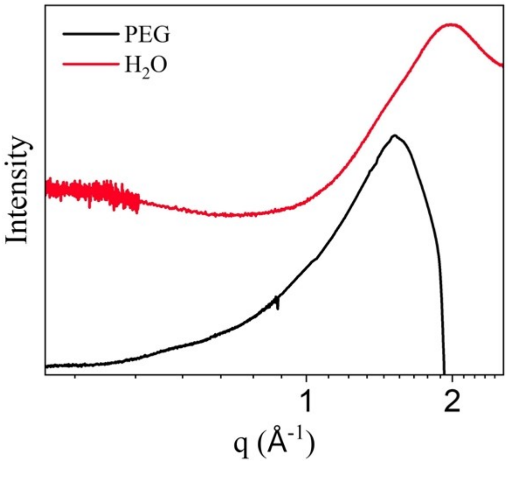

Figure S10. SAXS spectra for water and PEG solvent.

Table S1. Cumulative formation constants for metal complexes with chloride.

Metals	**Log β_1**	**Log β_2**	**Log β_3**	**Log β_4**	**Ref.**
Manganese (II)	-0.61				[2]
Iron (II)	0.015[a]	-1.25[a]		-4.1[a]	[3]
Copper (II)	4.0	4.7	2.0	0.23	[4]
Zinc (II)	0.43	0.61	0.53	0.20	[5]

[a]They were measured at 60 °C.

As shown in **Table S1**, which enlists the cumulative formation constants for chloro-metal complex ions, the formation of $[FeCl_4]^{2-}$ is less favorable compared to $[ZnCl_4]^{2-}$. This difference stems from the electronic configuration of Fe^{2+}, which, with a high-spin d^6 configuration, tends to form octahedral hydrated complexes rather than tetrahedral ones with halides. Thus, the coordination environment of Fe^{2+} is more labile due to the weak interactions between Fe^{2+} and aqua ligands, where some of the aqua ligands can be swapped by PEG as the invading ligands, leading to alterations in its coordination shell.

In contrast, Zn^{2+} has a d^{10} configuration, and with a full d-shell, the interactions between Zn^{2+} and its ligands are mainly through its empty 5s and 5p orbitals, which can be conveniently considered as sp^3 hybridization, thus favoring the T_d coordination of $[ZnCl_4]^{2-}$ with a relatively large formation constant. Furthermore, Zn^{2+} ions are small, which does not provide ample room for the bulky PEG ligands. Consequently, PEG cannot easily modify the coordination environment of Zn^{2+} because these tetrahedral complexes are less susceptible to coordination by PEG.

Table S2. Information of transition metal chloride electrolytes.

Electrolyte	**Oxidation State**	**Electron Configuration**	**Preferred geometry**	**Note**
$MnCl_2$	+2	High-spin d^5	O_h	High-spin d^5 and large ions favor O_h coordination[6]
$FeCl_2$	+2	High-spin d^6	O_h	High-spin d^6 large ions favor O_h coordination[7]
$CuCl_2$	+2	d^9	T_d	d^9 configuration with strong Jahn-Teller distortion favors T_d[8]
$ZnCl_2$, $ZnBr_2$, $Zn(OTf)_2$	+2	d^{10}	T_d	With a full d-shell, small Zn^{2+} favors T_d coordination with its "sp^3 hybridization[9]

$MnCl_2$: Manganese: +2 with a d^5 high-spin electronic configuration.

$FeCl_2$: Iron: +2 with a d^6 high-spin electronic configuration.

$CuCl_2$: Copper: +2 with a d^9 electronic configuration.

$ZnCl_2$/$ZnBr_2$/ $Zn(OTf)_2$: Zinc: +2 with a d^{10} configuration.

Next, the crystal field stabilization energy (CFSE) can be considered:

Mn^{2+}(d^5)

As for Mn^{2+}, its CFSE is zero in high-spin Oh coordination. Its CFSE is also zero in Td symmetry, but the overall Td ligand field is weaker, and the **Oh field is more stabilizing overall** due to greater ligand interactions. Thus Mn^{2+} favors Oh coordination.

Fe^{2+}(d^6)

Its CFSE is negative and larger when it is Oh rather than Td. Furthermore, the radius of Fe^{2+} is larger than Zn^{2+}, which favors Oh than Td geometry.

Cu^{2+} (d^9)

The d^9 configuration leads to Jahn-Teller distortion in Oh complexes, which often favors square-planar geometries with coordination with strong-field ligands. With chloride, Cu^{2+} readily forms tetrahedral $[CuCl_4]^{2-}$, rendering it less sensitive to the Jahn-Teller distortion.

Zn^{2+} (d^{10})

With a full d-shell, the interactions between Zn^{2+} and its ligands are mainly through its empty 5s and 5p orbitals, which can be conveniently considered as sp^3 hybridization, thus favoring the Td coordination. Therefore, Zn^{2+} readily forms tetrahedral complexes such as $[ZnCl_4]^{2-}$ and $[ZnBr_4]^{2-}$.

In addition, the small ionic radii of Zn^{2+} render the Td coordination a better fit than Oh coordination.

Regarding the addition of PEG, the resulting corrosion potential, and the different behaviors of metal ions:

Since Cu^{2+} and Zn^{2+} can form stable tetrachloro complexes, PEG cannot participate in their first solvation shells. The addition of PEG decreases the corrosion potential due to the shear concentration decrease when the electrolyte is diluted upon its addition.

In contrast, Mn^{2+} and Fe^{2+} predominantly exist as Oh hydrated complexes. When PEG is added to these electrolytes, it modifies the solvation structures of these ions, as the newly obtained **synchrotron-based SAXS** results explicitly revealed (new **Figure 2**). The PEG modification can reduce the desolvation energy penalty required for the ions to escape from their solvation sheaths for plating. Consequently, the corrosion potentials increase for Mn^{2+} and Fe^{2+}, despite the lower concentrations of these ions in $MnCl_2$ and $FeCl_2$ electrolytes after PEG dilution.

Furthermore, OTf^- ions (triflate) are weakly coordinated due to their lower electron density, which allows the PEG modification of the solvation sheath of Zn^{2+} ions. This modification contributes to the positive shift in the corrosion potential observed in $Zn(OTf)_2$.

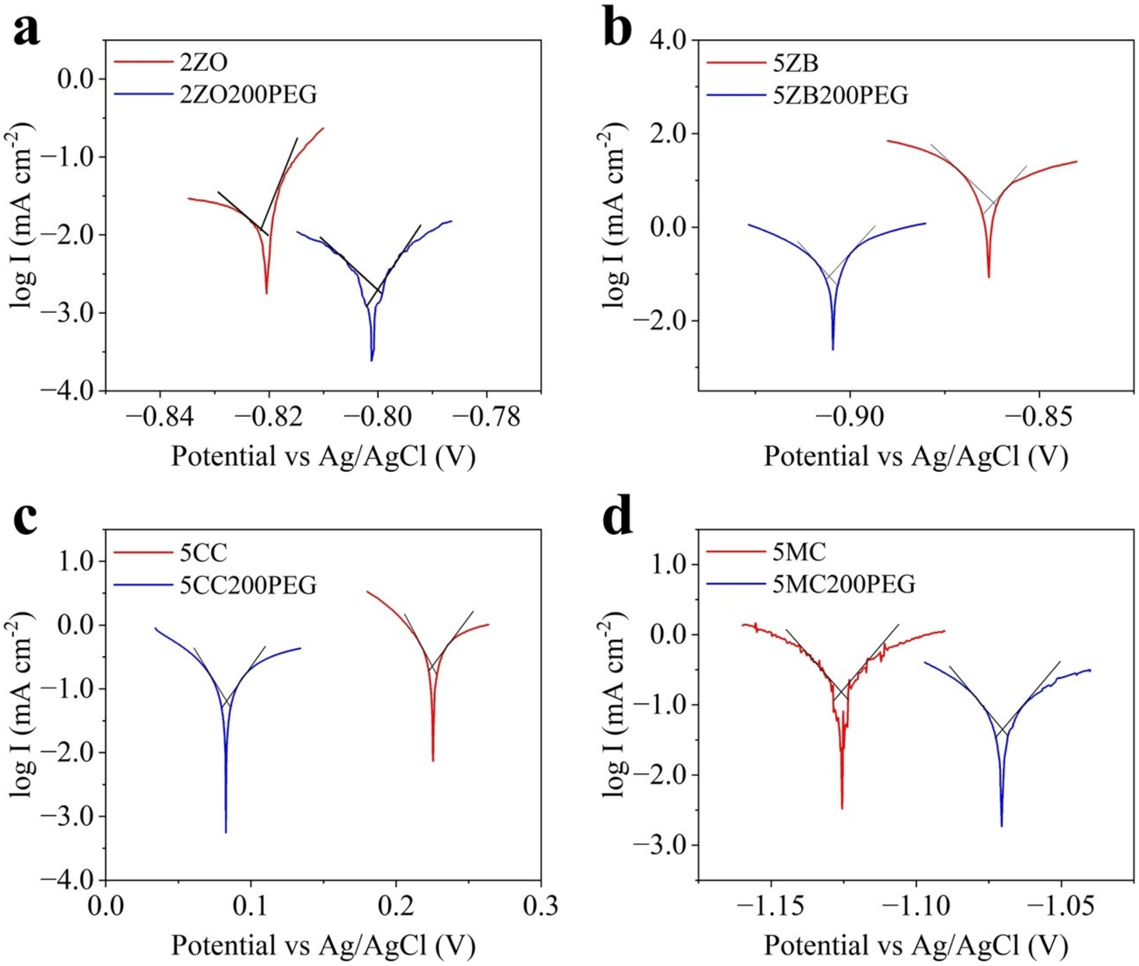

Figure S11. Tafel plots of three-electrode Swagelok cells with an Ag/AgCl reference electrode, scanned at 10 mV min^{-1}: (a and b) Zn foil (250 µm) serves as both the working and counter electrode. (c) Cu foil (10 µm) as both the working and counter electrode. (d) Mn free-standing film as both the working and counter electrodes.

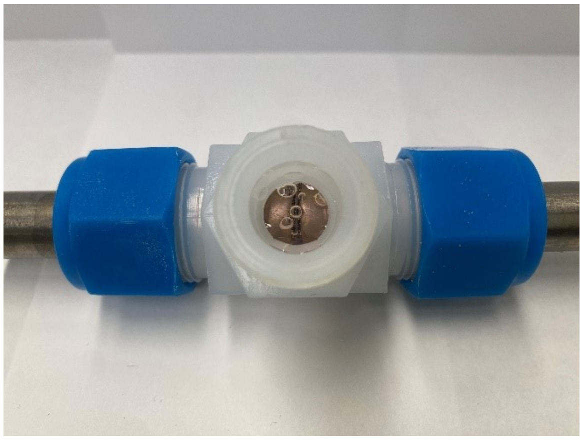

Figure S12. Photograph of the symmetric Mn || Mn Swagelok cell, featuring Mn free-standing film.

References

[1] B. D. Adams, J. Zheng, X. Ren, W. Xu, J. G. Zhang, *Adv. Energy Mater.,* **2018**, *8*, 1702097.

[2] C. H. Gammons, T. M. Seward, *Geochim. Cosmochim. Acta,* **1996**, *60*, 4295–4311.

[3] R. Zhao, P. Pan, *Can. J. Chem.,* **2001**, *79*, 131–144.

[4] M. A. Khan, M. J. Schwing-Weill, *Inorg. Chem.,* **1976**, *15*, 945.

[5] Y. Marcus, D. Maydan, *J. Phys. Chem.,* **1962**, *67*, 979–983.

[6] R. D. Dowsing, J. F. Gibson, M. Goodgame, P. J. Hayward, *J. Chem. Soc. A,* **1969**, 187–193.

[7] N. N. Greenwood, T. C. Gibb, *Mössbauer Spectroscopy*, **1971**.

[8] M. A. Halcrow, *Chem. Soc. Rev.,* **2013**, *42*, 1784–1795.

[9] C. Kutal, *Coord. Chem. Rev.,* **1990**, *99*, 213–252.